In Situ Grown AgI/$Bi_{12}O_{17}Cl_2$ Heterojunction Photocatalysts for Visible Light Degradation of Sulfamethazine: Efficiency, Pathway and Mechanism

Chengyun Zhou [a,b], Cui Lai [a,b], Piao Xu[a,b], Guangming Zeng [a,b,*], Danlian Huang [a,b,*], Chen Zhang [a,b], Min Cheng [a,b], Liang Hu [a,b], Jia Wan [a,b], Yang Liu[a,b], Weiping Xiong [a,b], Yaocheng Deng[a,b], Ming Wen [a,b]

[a] College of Environmental Science and Engineering, Hunan University, Changsha, Hunan 410082, China College of Environmental Science and Engineering, Hunan University, 8 South Lushan Road, Yuelu District, Changsha 410082, P.R. China

[b] Key Laboratory of Environmental Biology and Pollution Control, Ministry of Education, Hunan University, 8 South Lushan Road, Yuelu District, Changsha 410082, P.R. China

---

Corresponding authors

∗E-mail address: zgming@hnu.edu.cn (G.M. Zeng) Tel.: +86–731–88822754.

∗E-mail address: huangdanlian@hnu.edu.cn (D.L. Huang). Tel.: +86–731–88823701.

Abstract

Visible-light-driven photocatalysts attract great interest because they can utilize more sunlight for reactions than conventional photocatalysts. A novel visible-light-driven photocatalyst AgI/Bismuth oxychloride ($Bi_{12}O_{17}Cl_2$) hybrid was synthesized by hydrothermal-precipitation method. Several characterization tools, such as X-ray powder diffraction (XRD), scanning electron microscopy (SEM), high-resolution transmission electron microscopy (HRTEM), X-ray photoelectron spectroscopy (XPS) and UV−vis diffuse reflectance spectroscopy (DRS) were employed to study the phase structures, morphologies, and optical properties of the fabricated photocatalysts. These characterizations indicated that AgI nanoparticles were evenly distributed on the surface of $Bi_{12}O_{17}Cl_2$ and the heterostructures were formed. The photochemical characterizations demonstrated that the promoted separation of carrier transfer in the AgI/$Bi_{12}O_{17}Cl_2$ heterojunction was achieved. The degradation rate of sulfamethazine (SMZ) by AgI/$Bi_{12}O_{17}Cl_2$ was about 7.8 times and 35.2 times higher than that of pristine $Bi_{12}O_{17}Cl_2$ and BiOCl under visible light driven, respectively. It was also found that the amount of AgI in the AgI/$Bi_{12}O_{17}Cl_2$ composites played an important role in photocatalytic activity and the optimized ratio was 25%. The AgI/$Bi_{12}O_{17}Cl_2$ shows good catalytic stability and maintains similar reactivity after four cycles. Furthermore, the degradation intermediates of SMZ were identified by HPLC-MS, and the photocatalytic mechanism was proposed. These findings highlight the role of $Bi_{12}O_{17}Cl_2$ on contaminant elimination and open up avenues for the rational design of highly efficient photocatalysts.

Keywords: AgI/$Bi_{12}O_{17}Cl_2$, Photocatalytic degradation, Sulfamethazine wastewater, Heterojunctions.

Introduction

Chemicals such as pharmaceuticals (e.g., antibiotics, antidepressants, analgesics) and personal care products (e.g., shampoos, hair dyes, and soaps) have caused a new water quality issue.[1-6] Recently, sulfonamide antibiotics were classified as a priority risk group due to their high toxicity to bacteria at low concentrations and combined with their potential to cause resistance among natural bacterial populations.[7-9] Many studies found that conventional wastewater treatment plant can only partially remove antibiotics (20–90%).[10] A number of physical adsorption,[11-16] chemical reactions,[17-20] and biological degradation[21-22] methods have been applied to remove contaminant in wastewater. Pollutants can be migrated by physical adsorption, but cannot be completely eliminated. Biodegradation usually takes a long period of time and is often used to treat low concentrations of contaminants. Chemical reaction outcome can also be considered as contaminants.[23] There are even some evidence that these degradation products can be as active and/or toxic as their parent.[24]

In response to the increasing pollution issues, Semiconductor photocatalysis as a green technology has garnered particular attention. A lot of photocatalysts like TiO_2,[25-26] $g\text{-}C_3N_4$,[27-28] CdS,[29] and $SrTiO_3$[30] were explored for photocatalysis. Recently, bismuth-based materials are widely applied for the degradation of pollutant and water splitting.[31] Bismuth oxychloride (BiOCl), a wide band gap (about 3.3 eV) photocatalyst, has recently attracted considerable attention due to its good activity.[32-34] Especially, the layered structure feature of BiOCl can promote the effective separation of the photoinduced electron–hole pairs, which is an important factor for photocatalysis.[35-36] The BiOCl photocatalyst exhibited high activity on pollutant degradation under UV light. Zhang has explored facet-controllable of BiOCl, which offered superior activity on indirect dye photosensitization degradation under visible light.[37] Although many achievements have been reported, it is difficult to further narrow the band gap of BiOCl. Therefore, the strategy to reduce the band gap still needs to be explored.

Density functional theory (DFT) calculations suggest that an effective measure to decrease the band gap is to change the relative atomic ratios of BiOCl, such as $Bi_{12}O_{17}Cl_2$.[38-42] $Bi_{12}O_{17}Cl_2$ has the nanosheet structure with $Bi_{12}O_{17}^{2+}$ and Cl_2^{2-} layers.[43] With a relative small band gap (2.2-2.4 eV), $Bi_{12}O_{17}Cl_2$ can absorb visible light and be applied to degraded organic contaminants in water.[44] Nevertheless, the photocatalytic activity of $Bi_{12}O_{17}Cl_2$ is limited due to the high recombination rate of the photogenerated electron-hole pairs. Coupling $Bi_{12}O_{17}Cl_2$ with other semiconductors to form a heterojunction is an effective method to enhance the photocatalytic property of $Bi_{12}O_{17}Cl_2$. On the other hand, silver iodide (AgI) is a photosensitive material used in photography field. Recently, AgI has attracted wide attention due to the excellent photocatalytic property. But the micro sized AgI is unstable and can be reduced to the Ag^0 in light irradiation.[45-46] It has been found that a good substrate to disperse AgI could improve the stability and photoactivity of pure AgI, such as AgI/$Bi_2O_2CO_3$,[47] AgI/BiOI,[48] and AgI/CeO_2.[45] Furthermore, the corresponding conduction band of AgI is suitable for producing super oxygen species and enhancing the photooxidation ability. Therefore, the AgI/$Bi_{12}O_{17}Cl_2$ hybrid materials are expected to make up the shortcoming of the pure AgI and $Bi_{12}O_{17}Cl_2$. In addition, to the best of our knowledge, there has been no report about the AgI/$Bi_{12}O_{17}Cl_2$ hybrid materials and their application in the environment treatment field.

In this work, AgI/$Bi_{12}O_{17}Cl_2$ hybrid photocatalysts were fabricated via deposition-precipitation process. Different wt% (14%, 25%, 40%) of AgI were loaded on $Bi_{12}O_{17}Cl_2$ and the samples were denoted as x% AgI/$Bi_{12}O_{17}Cl_2$ (where x% = wt% of AgI from initial concentration of $Bi_{12}O_{17}Cl_2$). Sulfamethazine (SMZ), which belongs to the sulfonamide group of antibiotics, was chosen as the target pollutant. The morphology structures, optical properties, photoelectrical properties and photocatalytic activities of photocatalysts were fully validated. Furthermore, the possible degradation mechanism by AgI/$Bi_{12}O_{17}Cl_2$ composite was proposed. This work provides insight into the guideline of photocatalytic AgI/$Bi_{12}O_{17}Cl_2$ design and lays the groundwork for the application of AgI/$Bi_{12}O_{17}Cl_2$ as an efficient, stable, and low-cost visible light photocatalyst in wastewater treatment.

Experimental section

Materials. The bismuth nitrate pentahydrate ($Bi(NO_3)_3 \cdot 5H_2O$), ammonium chloride (NH_4Cl), ethylene glycol (EG), sodium hydroxide (NaOH), silver nitrate ($AgNO_3$) and potassium iodine (KI) were purchased from Sinopharm Chemical Reagent Corp, P. R. China. All chemicals were analytical grade and used as received without further purification. These aqueous solutions were prepared with ultrapure water (18.25 MΩ cm^{-1}) obtained from Millipore system.

Preparation of catalysts. The $Bi_{12}O_{17}Cl_2$ was fabricated by a previously reported method with minor modifications.[49] In a typical procedure, 0.97 g (2 mmol) $Bi(NO_3)_3 \cdot 5H_2O$ was dissolved in 10 mL EG. After 5 min stirring and 5 min sonication, the homogeneous solution was obtained. Then, 0.32 g (6 mmol) NH_4Cl and 0.80 g (20 mmol) NaOH were added to 60 mL distilled water under vigorous stirring for 10 min. The mixture was then poured into a 100 mL Teflon-lined stainless autoclave and heated at 140 °C for 12 h under the autogenous pressure. The resultant precipitate was collected and washed consecutively with deionized water and ethanol to remove residual ions. The final product was dried at 80 °C in air.

The AgI/$Bi_{12}O_{17}Cl_2$ heterojunction was fabricated by an *in situ* deposition-precipitation procedure. Typically, 0.70 g of $Bi_{12}O_{17}Cl_2$ was dispersed in 50 mL of deionized water under ultrasonic processing. Then, 0.17 g (1 mmol) $AgNO_3$ was added into the solution with the AgI amount in the composite set at 25 %. After the solution was stirred in dark for 1 h, a stoichiometric amount of KI was slowly added into the suspension above. The suspension was stirred for another 1 h to synthesize the samples. The resulting precipitates were washed with deionized water and absolute ethanol several times and then dried at 70 °C. A series of AgI/$Bi_{12}O_{17}Cl_2$ composites with different mass ratios of AgI and $Bi_{12}O_{17}Cl_2$ were prepared by changing the amounts of AgI and marked as 14%, 25%, and 40%. As a reference, the pristine AgI was prepared without adding $Bi_{12}O_{17}Cl_2$ under the same conditions.

Characterization methods. The crystal phase of the samples was determined by a D/max-2500 X-ray diffractometer (XRD; Rigaku, Japan) using Cu $K\alpha$ radiation ($\lambda = 0.15406$ nm) in the region of 2θ from 5° to 80°. X-ray photoelectron spectrum (XPS) of the samples was obtained by using an ESCALAB 250Xi spectrometer (Thermo Fisher, USA) with Al $K\alpha$ radiation ($h\nu = 1486.6$ eV). The UV–vis diffuse reflectance spectra (DRS) were performed on a UV–vis spectrophotometer (Cary 300, USA) with an integrating sphere. The photoluminescence (PL) spectra were recorded with Hitachi F-7000 fluorescence spectrophotometer at an excitation wavelength of 365 nm. Their morphology was examined by transmission electron microscope (TEM, JEOL JEM-2100F). The total organic carbon (TOC) was applied to analyze the mineralization degree of organic contaminants on Analytik Jena AG (Multi N/C 2100). The electron spin resonance (ESR) signals of radicals spin-trapped by spin-trapping reagent 5, 5-dimethyl-l-pyrroline N-oxide (DMPO) and

2,2,6,6-Tetramethylpiperidinooxy (TEMPO) were examined on a Bruker ER200-SRC spectrometer under visible light irradiation (λ> 420 nm).

Photocatalytic experiments. In order to evaluate the photocatalytic activity of prepared samples, photocatalytic removal of SMZ was carried out under visible light irradiation using a 300 W Xe lamp (CELHXF300, China) with a 420 nm cut filter. Typically, the photocatalyst (50 mg) was suspended in 50 mL water containing SMZ (10 mg L^{-1}). Subsequently, the solution was magnetically stirred for 1 h in dark to ensure the establishment of equilibrium between adsorption and desorption. After that, the mixture was exposed to visible light, and 1 mL of solution was taken out at given time interval, centrifuged, filtrated by 0.22 μm membrane filter and analyzed. The SMZ concentration was determined using an HPLC Series 1100 (Agilent, Waldbronn, Germany) equipped with a UV detector. The Column was a C-18 column (4.6 × 250 mm) at the temperature of 30 °C. The mobile phase was water–acetonitrile (80:20, v/v) with 0.1% acetic acid at the flow rate 1 mL min^{-1}. The sample volumes for injection were all 20 μL and the wavelength of detector was 270 nm. A liquid chromatography mass spectrometry (LC–MS) (Agilent 1290/6460, Triple Quad MS, USA) was used to determine the intermediate products from SMZ degradation. The isocratic mobile phase was prepared by using 0.1% acetic acid and acetonitrile with the ratio of 70:30 (v/v), which was set at a flow rate of 0.1 mL min^{-1}. The gradient mobile phase was the combination of acetonitrile and 0.1% acetic acid. The gradient elution was programmed as follows: 0-1 min, 10% acetonitrile; 1-12 min, 10-90% acetonitrile; 12-15 min, 90% acetonitrile; 15-20 min, 10-90% acetonitrile.

Electrochemical measurements. To prepare the electrodes, the catalyst was dispersed in Nafion solution (0.5 wt%) to form a 10 mg mL^{-1} solution. 100 μL of the resultant solution was then dip-coated on the pretreated fluorine-doped tin oxide (FTO) surface and allowed for drying in a vacuum oven for 24 h at room temperature. The photocurrent measurements were conducted on an electrochemical workstation (CHI660D Instruments) in a standard three-electrode system with the catalyst coated electrode as the working electrode, a Pt electrode (40×0.55 mm, 99%) as the counter electrode and the Ag/AgCl electrode as the reference electrode. The 300W xenon lamp with a 420 nm cutoff filter was utilized as the light source for the photocurrent (I-t) measurements. The electrochemical impedance spectroscopy (EIS) was also performed in Na_2SO_4 aqueous solution with the above three-electrode system.

Results and discussion

Catalysts characterization. The XRD patterns of investigated samples were shown in Figure 1. The patterns of pristine $Bi_{12}O_{17}Cl_2$ and AgI agreed well with the standard phase of $Bi_{12}O_{17}Cl_2$ (JCPDS card No. 37-0702) and the standard cubic phase of AgI (JCPDS card No. 09-0374), respectively.[46, 50] Characteristic peaks at 22.32°, 23.71°, 39.13°, and 46.31° which were respectively corresponded to lattice plane (100), (002), (110), and (112) of AgI, were all observed on AgI/$Bi_{12}O_{17}Cl_2$. With the increase of the AgI amount, the diffraction peaks (115), (117), (200), and (220) of $Bi_{12}O_{17}Cl_2$ are also present in the pattern of AgI/$Bi_{12}O_{17}Cl_2$ and gradually get weaker. These results indicate that the growth of $Bi_{12}O_{17}Cl_2$ has been restrained by AgI in the formation of the crystals.[51]

The composition and chemical status of the as-prepared samples were also confirmed by XPS technique. As shown in Figure 2a, Ag 3d, I 3d, Bi 4f, O 1s, and Cl 2p was detected in the spectrum of 25% AgI/$Bi_{12}O_{17}Cl_2$. The doublet peaks of Ag $3d_{5/2}$ and Ag $3d_{3/2}$ could be divided into two individual peaks. The peak of Ag 3d was unsymmetrical, which indicated that there were two different valence states of silver in the catalysts. The peaks at 367.6 eV and 373.5 eV were attributed to Ag^+ in AgI, and those at 368.6 eV and 374.5 eV were assigned to Ag^0 species (Figure 2b).[52] The reason of negative shift of Ag 3d XPS on going from 0 to +1 was that the Ag^+ was partially reduced to the Ag^0 during the synthesis process for AgI.[53] The peak at 618.6 eV (I $3d_{5/2}$) and 630.9 eV (I $3d_{3/2}$) in the I 3d region are assigned to I^- in AgI (Figure 2c).[48] The binding energies of Bi $4f_{5/2}$ and Bi $4f_{7/2}$ are 164.2 and 158.9 eV for pristine $Bi_{12}O_{17}Cl_2$, respectively (Figure 2d). However, AgI/$Bi_{12}O_{17}Cl_2$ exhibits two distinct peaks of Bi $4f_{5/2}$ and Bi $4f_{7/2}$ separately locating at 164.9 and 159.3 eV, respectively. Comparing with pristine $Bi_{12}O_{17}Cl_2$, a slight binding energy left–shift of Bi 4f peaks (164.2 eV shifts to 164.9 eV, 158.9 eV shifts to 159.3 eV) occurred over AgI/$Bi_{12}O_{17}Cl_2$, indicating that the chemical coordination environment of Bi^{3+} ions may be changed.[51, 54] Figure 2e shows the Cl 2p peak of $Bi_{12}O_{17}Cl_2$. It exhibits two main peaks with binding energies at 199.1 and 197.3 eV, which can be ascribed to Cl $2p_{1/2}$ and Cl $2p_{3/2}$, respectively. [36] The O 1s fit well with the peak at 529.5 eV, which belongs to bismuth oxygen bond in $Bi_{12}O_{17}Cl_2$ (Figure 2f). The obtained results were in good agreement with the XRD analysis.

The SEM images of morphology and EDS mapping of $Bi_{12}O_{17}Cl_2$, and AgI/$Bi_{12}O_{17}Cl_2$ were showed in Figure 3. The SEM images (Figure 3a) reveal that the sample possessed nanolayer structure. The nanoparticles of AgI homogenously disperse on the layer of $Bi_{12}O_{17}Cl_2$ (in Figure

3b and 3c), which was further confirmed by TEM. The EDS data shown in Figure 3d-h confirm the existence of Ag, I, Bi, O, and Cl were in the AgI/$Bi_{12}O_{17}Cl_2$.

The structures of the AgI, $Bi_{12}O_{17}Cl_2$, and AgI/$Bi_{12}O_{17}Cl_2$ were further studied by TEM and HRTEM in Figure 4. It can be seen from Figure 4a that pristine AgI composes of a large scale of nanoparticles with a diameter ranging from 50 to 200 nm. As can be seen from Figure 4b, the as-prepared pristine $Bi_{12}O_{17}Cl_2$ sample reveals a clearly flat layer structure. The nanolayer has a width and length range of 50-100 nm and 0.2-1.0 μm, respectively. As shown in Figure 4c，a batch of nanoparticle developed from AgI, which deposited on the surface of the $Bi_{12}O_{17}Cl_2$ nanosheets in AgI/$Bi_{12}O_{17}Cl_2$. In Figure 4d, the d-spacing of lattice spacing of $Bi_{12}O_{17}Cl_2$ is 0.306 and 0.271 nm corresponding to (117) and (200) interlayer spacing respectively, indicating there is no change in the lattice structure of $Bi_{12}O_{17}Cl_2$ after loading AgI.[12] Also, the d spacing of AgI is 0.231 nm in AgI/$Bi_{12}O_{17}Cl_2$, corresponding to the (110) plane. The HRTEM and SAED of single AgI and single $Bi_{12}O_{17}Cl_2$ were depicted in Figure S1. The results indicated that the heterojunction was constructed between AgI and $Bi_{12}O_{17}Cl_2$ in the AgI/$Bi_{12}O_{17}Cl_2$ with interaction interfaces.

Optical absorption properties and photoelectrical properties. UV–Vis diffuse reflectance spectroscopy (DRS) was conducted to evaluate the band gap energies (E_g) of as-synthesized samples. As shown in Figure 5a, the absorption edge of the pristine $Bi_{12}O_{17}Cl_2$ and AgI were located at about 520 nm and 475 nm, respectively. With increasing the mass ratio of AgI, the optical absorption edges were still located at between 475 nm and 520 nm, indicating that all the AgI/$Bi_{12}O_{17}Cl_2$ composites possessed visible light response. Compared with pristine $Bi_{12}O_{17}Cl_2$ and AgI, the optical absorption edges of 25% AgI/$Bi_{12}O_{17}Cl_2$ composites were red-shifted obviously. Their band gap were calculated using the following equation (Eq. 1):

$$\alpha hv = A(hv - E_g)^{n/2} \quad (1)$$

Where α, *h, v*, E_g, and A are the absorption coefficient, Planck's constant, light frequency, band gap energy, and a constant, respectively; n is determined by the type of optical transition of a semiconductor (n=1 for direct transition and n=4 for indirect transition).[55] The optical transition of AgI was direct and the band gap energy of AgI was measured at 2.78 eV (Figure 5b). However, the $Bi_{12}O_{17}Cl_2$ is an indirect semiconductor. As shown in the Figure 4c, the $Bi_{12}O_{17}Cl_2$ was estimated from a plot of $(\alpha hv)^2$ as a function of the photon energy (*hv*) to be approximately 2.41 eV.

The photoluminescence (PL) spectra of the samples were studied in Figure S2. All samples exhibit an emission peak centered at about 680 nm. Compared with pristine $Bi_{12}O_{17}Cl_2$ and AgI, the AgI/$Bi_{12}O_{17}Cl_2$ composites show significant quenching of the PL. These results revealed that AgI/$Bi_{12}O_{17}Cl_2$ exhibited the best activity in terms of charge carrier density, hole-electron separation, and charge transportation than $Bi_{12}O_{17}Cl_2$ and AgI.

I-t property has been verified to be an efficient approach to reflect the photogenerated charge separation in the heterojunction photocatalysts.[56-57] In Figure 6a, all samples presented good reproducibility of photocurrent under visible light. The photocurrent of AgI/$Bi_{12}O_{17}Cl_2$ was nearly 4 times higher than pristine $Bi_{12}O_{17}Cl_2$. The enhancement of photocurrent illustrated that the mobility of the charge carriers was promoted. This result suggested that the improved charge separation of carriers were realized in the heterojunction of AgI/$Bi_{12}O_{17}Cl_2$.

EIS is a versatile technique used to characterize phenomena such as corrosion, fuel cells and batteries.[58-59] This technique could be used to explain the electron-transfer efficiency at the electrodes.[60] For further verifying the efficient separation of carriers, we measured the EIS of AgI,

$Bi_{12}O_{17}Cl_2$ and AgI/$Bi_{12}O_{17}Cl_2$ in the Figure 6b. The AgI/$Bi_{12}O_{17}Cl_2$ displays smallest arc radius in the EIS Nyquist plot than the pristine AgI and $Bi_{12}O_{17}Cl_2$. It demonstrates that AgI/$Bi_{12}O_{17}Cl_2$ has low interfacial layer resistance, which agrees with the results of PL and I-t.

Photocatalytic activity. The photocatalytic activities of the AgI/$Bi_{12}O_{17}Cl_2$ composites were measured by decomposing SMZ under visible light irradiation. SMZ is a kind of organic contaminant, which is difficult to be decomposed.[61-62] Before irradiation, dark adsorption experiment was carried out to discuss the adsorption efficiency of the samples. As revealed in Table S1, there was no increasing adsorption after 30 min dark adsorption. In our experiment, 60 min dark adsorption was enough to reach the adsorption equilibrium between photocatalyst and SMZ. Figure 7a shows the photodegradation of SMZ as a function of irradiation time over different photocatalysts. After irradiation for 60 min, the SMZ photodegradation did not occur in the absence of the photocatalyst, while the pristine AgI and $Bi_{12}O_{17}Cl_2$ achieved the degradation efficiencies of 38.51% and 45.39%, respectively. All of the heterojunction samples (including 14%, 25%, 40% AgI/$Bi_{12}O_{17}Cl_2$) exhibited enhanced photocatalytic activities greatly. It suggested that AgI amounts played a crucial role in the photocatalytic activity and a small amount of AgI (14%) over $Bi_{12}O_{17}Cl_2$ could lead to a sharp increase of SMZ decomposition from 45.39% to 83.26%. As the AgI amount increased to 25%, the highest photocatalytic activity was achieved, at which 96.15% of SMZ were decomposed. However, the photocatalytic activity decreased when the AgI amount rose to 40%. This result may due the excess of AgI facilitate the recombination of photoinduced carriers in the AgI/$Bi_{12}O_{17}Cl_2$ composite. According to the above results, the optimized amount of AgI in the AgI/$Bi_{12}O_{17}Cl_2$ composites was 25%. Besides, the photocatalytic performance of a mechanical mixture of 25% AgI/$Bi_{12}O_{17}Cl_2$ was also investigated. The degradation efficiency (83.15%) of mechanical mixture is much lower than that obtained by using 25% AgI/$Bi_{12}O_{17}Cl_2$, suggesting that heterojunction may formed between AgI and $Bi_{12}O_{17}Cl_2$ through the intimate interfacial contact.

The degradation kinetics of SMZ was investigated by fitting the experimental data to the following pseudo-first-order kinetics equation:

$$-\ln(C_t/C_0)=kt \qquad (2)$$

Where C_t is the instant of SMZ concentration, C_0 is the initial of SMZ concentration; k (min^{-1}) is the apparent reaction rate constant. The entire sample could be fitted well by the pseudo-first-order kinetics model with high fitting coefficient. In Figure 7b, the results showed that the highest k value for 25% AgI/$Bi_{12}O_{17}Cl_2$ was 0.070 min^{-1}, which was 7.8, 7.0 and 35 times higher than that of pristine $Bi_{12}O_{17}Cl_2$ (0.009 min^{-1}), AgI (0.010 min^{-1}) and BiOCl (0.002 min^{-1}), respectively.

Various initial concentrations of SMZ (10-50 mg L^{-1}) were used to test the activities of the 25% AgI/$Bi_{12}O_{17}Cl_2$, and the results were depicted in Figure 7c. With the increasing concentration, the removal efficiency decreased. The efficiency of 25% AgI/$Bi_{12}O_{17}Cl_2$ dropped from 96.15% (10 mg L^{-1}) to 43.26% (50 mg L^{-1}) in 1h irradiation. As shown in Figure 7d, all samples could be fitted well by the pseudo-first-order kinetics model with high coefficients. This negative effect was explained that a certain amount of AgI/$Bi_{12}O_{17}Cl_2$ can generate the same active species to remove SMZ. Lower concentration of initial pollutants can achieve higher removal rate at the same time. Therefore, dilution was essential in the pretreatment of practical wastewater treatment.

The effective mineralization of organic compounds to avoid secondary pollution of photocatalytic technology is very important in the practical applications. In this system, TOC was chosen as a mineralization index and the time independence of the TOC data in SMZ solution over 25% $AgI/Bi_{12}O_{17}Cl_2$ during the photocatalytic process is shown in Figure 8. As can be seen from Figure 8, the TOC of 25% $AgI/Bi_{12}O_{17}Cl_2$ was decreased with the increasing of illumination time. After 120 min irradiation, over 60% of TOC was eliminated, indicating that the SMZ could effectively mineralized by the as-prepared 25% $AgI/Bi_{12}O_{17}Cl_2$ under visible light irradiation. Furthermore, the TOC of pristine $Bi_{12}O_{17}Cl_2$ was also studied in Figure S4.

From the viewpoint of practical applications, the $Bi_{12}O_{17}Cl_2$ and 25% $AgI/Bi_{12}O_{17}Cl_2$ composite were selected to evaluate the reusability of the as-prepared composites. As shown in Figure 9, the $AgI/Bi_{12}O_{17}Cl_2$ showed a good catalytic stability and maintained a similar reactivity after four cycles. Compared to $AgI/Bi_{12}O_{17}Cl_2$, the degradation efficiency of $Bi_{12}O_{17}Cl_2$ exist a significant loss. The composition of the recycled $AgI/Bi_{12}O_{17}Cl_2$ composite was also characterized by XRD. As shown in Figure S3, the XRD patterns of the $AgI/Bi_{12}O_{17}Cl_2$sample after the photocatalytic reactions reveal that its crystal structure remained unchanged. Therefore, the $AgI/Bi_{12}O_{17}Cl_2$ is a stable and efficient photocatalyst for degradation of organic pollutants, which is helpful to be applied in practical application in future.

To understand the photodegradation mechanism of SMZ, the free radical, holes (h^+), superoxide radical anions ($\bullet O_2^-$) and hydroxyl radicals (•OH) trapping experiments were carried out to identify the main active species taking part in the degradation process. According to the previous report, different scavengers (ethylenediaminetetraacetic acid disodium salt as a hole scavenger, isopropyl alcohol as an •OH scavenger and benzoquinone as an $•O_2^-$ scavenger) could be used to trap the free radicals.[63-65] As shown in the Figure 10a, the photodegradation rates of pristine $Bi_{12}O_{17}Cl_2$ were obviously suppressed with the presence of benzoquinone (BQ) or ethylenediaminetetraacetic acid disodium (EDTA-2Na). The removal efficiency of SMZ decreased from 52.23% to 18.12% with the addition of 1mM EDTA-2Na. The addition of 1mM isopropyl alcohol (IPA) had slightly suppressed the decomposition of SMZ, implying that •OH played an insignificant role in the decomposition of SMZ under visible light irradiation. It demonstrated that the photogenerated holes and $•O_2^-$ were the predominant oxidant in the photocatalytic degradation of SMZ for pristine $Bi_{12}O_{17}Cl_2$. As shown in the Figure 10b, the photocatalytic activity of $AgI/Bi_{12}O_{17}Cl_2$ was greatly suppressed by the addition of these three scavengers. The inhibition efficiencies for the removal of SMZ were estimated to be 30.53% for EDTA-2Na, and 25.89% for BQ, respectively. Thus, it could be deduced that holes, $•O_2^-$, and •OH were in the $AgI/Bi_{12}O_{17}Cl_2$.

Moreover, in order to further confirm the main active species in this catalytic system under visible irradiation, the ESR spin-trap with DMPO technique was performed on illuminated $AgI/Bi_{12}O_{17}Cl_2$ composite (Figure 10c and d).[66] As shown in Figure 10c, four obvious signals with $AgI/Bi_{12}O_{17}Cl_2$ in methanol were produced, which could be assigned to DMPO-$•O_2^-$ under light illumination. There is no $•O_2^{--}$ signal in the dark, but an increasing signal of DMPO-$•O_2^{--}$ could be observed with visible light irradiation. Moreover, the signal of •OH was also detected in DMPO system when exposed to light in Figure 10d. The results of ESR were well consistent with the trapping experiment. It revealed that the degradation mechanism of $AgI/Bi_{12}O_{17}Cl_2$ composite has been changed compared with that of pristine $Bi_{12}O_{17}Cl_2$.

Degradation pathway of SMZ by AgI/$Bi_{12}O_{17}Cl_2$. The removal efficiency of AgI/$Bi_{12}O_{17}Cl_2$ was also shown in Figure S5. The SMZ (t=3.89 min) concentration gradually decreased with the increase of irradiation time and became undetectable after 120 min irradiation. It indicated that most of the pollutants were mineralized to small inorganic molecules, like CO_2 and H_2O under the photocatalytic degradation process after 120 min irradiation, further revealing the strong photo-oxidation capability of AgI/$Bi_{12}O_{17}Cl_2$ heterojunction.

To further understand the degradation mechanism of the SMZ (denoted as P1) in the AgI/$Bi_{12}O_{17}Cl_2$ system under visible irradiation, HPLC-MS were used to identify the degradation intermediates. As it was shown in Figure S6, SMZ and other four main degradation products were observed. The molecular weight for P1 is 278.33. Since the Electrospray ionization (ESI) source was used in HPLC-MS, the m/z was the $M+H^+$. With the prolongation of irradiation time, the concentration of P1 (m/z value of 279.3) decreased gradually. Meanwhile, the four intermediates including P2 (m/z value of 309.0), P3 (m/z value of 339.3), P4 (m/z value of 215.1), and P5 (m/z value of 124.0) were formed in 30 min irradiation. After 120 min irradiation, the intermediate P2 disappeared, and the concentration of intermediates including P3, P4, and P5 were decreased. As shown in Figure 11, three degradation pathways have been proposed as following, (1) the initial product of SMZ was P2 (m/z value of 309.0), which was formed through the oxidation of amidogen on the benzene ring. Subsequently, the P3 (m/z value of 339.3) was produced by further oxidation via carboxylation of the methyl group; (2) The P4 (m/z value of 215.1) was produced by the decay of pyrimidine ring forming urea in SMZ; (3) The P5 (m/z value of 124.0) was produced by the hydroxyl radicals attack on the SMZ which resulted in the cleavage of S-N bond on SMZ, and further formed the pyrimidine ring. The proposed reaction route has the correlation with the kinetic results. The concentration of SMZ was decreased rapidly in the first 60 min irradiation in Figure 8. At this time, the TOC removal rate was increased slowly due to the large molecular weight intermediates (like P2 and P3) generated. With the extension of irradiation time, the concentration of SMZ was in a low level and the intermediates (like P4 and P5) begin to decompose, then the TOC removal rate was increased rapidly. The degradation products did not accumulate during photocatalytic system and their concentrations were at a low level. These degradation products would decompose into small molecules, such as H_2O, CO_2, and NH_4^+.

Possible degradation mechanism. The high photocatalytic activity of the as-synthesized $AgI/Bi_{12}O_{17}Cl_2$ composites may be related to their unique band. Different conduction band (CB) and valence band (VB) levels can change the efficiency of charge transfer.[67] The Mott-schottky plots of pristine AgI and $Bi_{12}O_{17}Cl_2$ were showed in Figure S7a. The flat potentials of pristine AgI and $Bi_{12}O_{17}Cl_2$ were calculated to be -0.42 and -0.48 V versus the $Hg/HgCl_2$ electrode (SCE). And they were equivalent to -0.18 and -0.24 V versus the normal hydrogen electrode (NHE). The flat potential is almost equal to that of the Fermi level.[68] Besides, Figure S7b showed the VB-XPS spectra of pristine AgI and $Bi_{12}O_{17}Cl_2$. It showed that the gap between the Fermi level and VB was 1.49 eV for the AgI, while it was 1.74 eV for the $Bi_{12}O_{17}Cl_2$. So the VB of pristine AgI and $Bi_{12}O_{17}Cl_2$ were equal to 1.31 and 1.50 eV. According to the previous result, the band gap energy of AgI and $Bi_{12}O_{17}Cl_2$ was measured at 2.78 and 2.41 eV, respectively. So the CB of AgI and $Bi_{12}O_{17}Cl_2$ were found to be -1.47 and -0.91 eV, respectively. After AgI and $Bi_{12}O_{17}Cl_2$ contact, the higher Fermi energy of $Bi_{12}O_{17}Cl_2$ than AgI caused the energy bands of $Bi_{12}O_{17}Cl_2$ to bend upward and AgI to bend downward toward the interface to reach electrical equilibrium. Therefore, the possible mechanism was proposed based on above results.[47] As shown in Figure 12, under visible light irradiation, both AgI and $Bi_{12}O_{17}Cl_2$ could excite hole and electron, the electrons of the CB of AgI would transfer to the CB of the $Bi_{12}O_{17}Cl_2$ to reduce surface O_2 into the oxidize species •O_2^-. Then, parts of •O_2^- reacted with H^+ and generated H_2O_2, which was further excited by electrons and changed into •OH. The holes of the $Bi_{12}O_{17}Cl_2$ would be transferred to VB of AgI, and the holes of the VB of AgI could directly oxidize organic pollutants into small molecular. In this route, the electrons and holes could be separated efficiently, leading to the high photocatalytic activity of AgI/$Bi_{12}O_{17}Cl_2$. The active species, holes, •O_2^- and •OH, could further effectively degrade the target pollutant (SMZ) into more small intermediates or directly into end products (CO_2 and H_2O). Furthermore, the photogenerated electrons of AgI tend to migrating to the $Bi_{12}O_{17}Cl_2$, which may avoid the AgI reduced to Ag, and further enhanced the stability of AgI under visible irradiation.

Conclusions

In summary, a visible-light driven catalyst system has been developed using AgI and hydrothermal prepared $Bi_{12}O_{17}Cl_2$ as a photocatalyst to make contact heterostructure for efficient degradation of SMZ. The characterizations showed that AgI nanoparticles evenly distributed on the surface of $Bi_{12}O_{17}Cl_2$ and the heterostructures were formed. The degradation rate of SMZ by AgI/$Bi_{12}O_{17}Cl_2$ was about 7.8 times and 35.2 times higher than that of pristine $Bi_{12}O_{17}Cl_2$ and BiOCl under visible light driven, respectively. It was also found that the AgI amount in the AgI/$Bi_{12}O_{17}Cl_2$ composites played an important role in the corresponding photocatalytic properties and the optimized ratio was obtained at 25%. The dramatic enhancement in the visible light photocatalytic activity can be attributed to the effective photogenerated charge transfer at the interface of AgI and $Bi_{12}O_{17}Cl_2$. High photocurrent intensity, great mineralization ability, and excellent photostability were also obtained for the AgI/$Bi_{12}O_{17}Cl_2$ sample. The SMZ degradation pathway can be divided into three steps: cleaving, aromatic ring opening, and mineralizing. The photogenerated reactive species and degradation intermediates are identified, and a photocatalytic mechanism is proposed. Moreover, these composites could apply to other contaminant degradation in wastewater and treated effluent water.

Associated content

Supporting Information

TEM images, Photoluminescence, Mott-schottky plots, and XPS-VB of the prepared samples, photocatalytic degradation, TOC removal, HPLC-MS analysis of SMZ by the prepared samples.

Author information

Corresponding authors

∗E-mail: zgming@hnu.edu.cn (G.M. Zeng). Tel.: +86–731–88822754.

∗E-mail : huangdanlian@hnu.edu.cn (D.L. Huang). Tel.: +86–731–88823701.

Notes The authors declare no competing financial interest.

Acknowledgements

The authors would like to thank Ning Yan for his assistance with the TEM measurements， Jianjun Xu for help with SEM measurements, and Shuqu Zhang for his assistance with the DRS measurements. This study was financially supported by the Program for the National Natural Science Foundation of China (51579098, 51779090, 51709101, 51278176, 51521006, 51378190, 51408206), the National Program for Support of Top-Notch Young Professionals of China (2014), the Fundamental Research Funds for the Central Universities, Hunan Provincial Science and Technology Plan Project (No.2016RS3026), the Program for New Century Excellent Talents in University (NCET-13-0186), the Program for Changjiang Scholars and Innovative Research Team in University (IRT-13R17).

Reference

(1) Watkinson, A. J.; Murby, E. J.; Costanzo, S. D. Removal of antibiotics in conventional and advanced wastewater treatment: Implications for environmental discharge and wastewater recycling. *Water Res.* **2007,** *41* (18), 4164-4176, DOI: 10.1016/j.watres.2007.04.005.

(2) Watkinson, A. J.; Murby, E. J.; Kolpin, D. W.; Costanzo, S. D. The occurrence of antibiotics in an urban watershed: From wastewater to drinking water. *Sci. Total Environ.* **2009,** *407* (8), 2711-2723, DOI: 10.1016/j.scitotenv.2008.11.059.

(3) Huang, D.-L.; Wang, R.-Z.; Liu, Y.-G.; Zeng, G.-M.; Lai, C.; Xu, P.; Lu, B.-A.; Xu, J.-J.; Wang, C.; Huang, C. Application of molecularly imprinted polymers in wastewater treatment: a review. *Environ. Sci. Pollut. Res.* **2015,** *22* (2), 963-977.

(4) Huang, D.; Xue, W.; Zeng, G.; Wan, J.; Chen, G.; Huang, C.; Zhang, C.; Cheng, M.; Xu, P. Immobilization of Cd in river sediments by sodium alginate modified nanoscale zero-valent iron: Impact on enzyme activities and microbial community diversity. *Water Res.* **2016,** *106*, 15-25.

(5) Zeng, G.; Wan, J.; Huang, D.; Hu, L.; Huang, C.; Cheng, M.; Xue, W.; Gong, X.; Wang, R.; Jiang, D. Precipitation, adsorption and rhizosphere effect: The mechanisms for Phosphate-induced Pb immobilization in soils—A review. *J. Hazard. Mater.* **2017,** *339* (Supplement C), 354-367, DOI: https://doi.org/10.1016/j.jhazmat.2017.05.038.

(6) Hu, L.; Wan, J.; Zeng, G.; Chen, A.; Chen, G.; Huang, Z.; He, K.; Cheng, M.; Zhou, C.; Xiong, W.; Lai, C.; Xu, P. Comprehensive evaluation of the cytotoxicity of CdSe/ZnS quantum dots in Phanerochaete chrysosporium by cellular uptake and oxidative stress. *Environmental Science: Nano* **2017,** *4* (10), 2018-2029, DOI: 10.1039/C7EN00517B.

(7) Zhang, Y.; Zeng, G.-M.; Tang, L.; Huang, D.-L.; Jiang, X.-Y.; Chen, Y.-N. A hydroquinone

biosensor using modified core–shell magnetic nanoparticles supported on carbon paste electrode. *Biosens. Bioelectron.* **2007,** *22* (9-10), 2121-2126, DOI: 10.1016/j.bios.2006.09.030.

(8) Cheng, Y.; He, H.; Yang, C.; Zeng, G.; Li, X.; Chen, H.; Yu, G. Challenges and solutions for biofiltration of hydrophobic volatile organic compounds. *Biotechnol. Adv.* **2016,** *34* (6), 1091-1102, DOI: 10.1016/j.biotechadv.2016.06.007.

(9) Huang, D.; Liu, L.; Zeng, G.; Xu, P.; Huang, C.; Deng, L.; Wang, R.; Wan, J. The effects of rice straw biochar on indigenous microbial community and enzymes activity in heavy metal-contaminated sediment. *Chemosphere* **2017,** *174*, 545-553.

(10) Grandclement, C.; Seyssiecq, I.; Piram, A.; Wong-Wah-Chung, P.; Vanot, G.; Tiliacos, N.; Roche, N.; Doumenq, P. From the conventional biological wastewater treatment to hybrid processes, the evaluation of organic micropollutant removal: a review. *Water Res.* **2017**.

(11) Gong, J.-L.; Wang, B.; Zeng, G.-M.; Yang, C.-P.; Niu, C.-G.; Niu, Q.-Y.; Zhou, W.-J.; Liang, Y. Removal of cationic dyes from aqueous solution using magnetic multi-wall carbon nanotube nanocomposite as adsorbent. *J. Hazard. Mater.* **2009,** *164* (2-3), 1517-1522, DOI: 10.1016/j.jhazmat.2008.09.072.

(12) Xu, P.; Zeng, G. M.; Huang, D. L.; Feng, C. L.; Hu, S.; Zhao, M. H.; Lai, C.; Wei, Z.; Huang, C.; Xie, G. X.; Liu, Z. F. Use of iron oxide nanomaterials in wastewater treatment: A review. *Sci. Total Environ.* **2012,** *424*, 1-10, DOI: 10.1016/j.scitotenv.2012.02.023.

(13) Feng, Y.; Gong, J.-L.; Zeng, G.-M.; Niu, Q.-Y.; Zhang, H.-Y.; Niu, C.-G.; Deng, J.-H.; Yan, M. Adsorption of Cd (II) and Zn (II) from aqueous solutions using magnetic hydroxyapatite nanoparticles as adsorbents. *Chem. Eng. J.* **2010,** *162* (2), 487-494, DOI: 10.1016/j.cej.2010.05.049.

(14) Zhang, C.; Lai, C.; Zeng, G.; Huang, D.; Yang, C.; Wang, Y.; Zhou, Y.; Cheng, M. Efficacy of carbonaceous nanocomposites for sorbing ionizable antibiotic sulfamethazine from aqueous solution. *Water Res.* **2016,** *95*, 103-112, DOI: 10.1016/j.watres.2016.03.014.

(15) Zhong, S.; Zhou, C.; Zhang, X.; Zhou, H.; Li, H.; Zhu, X.; Wang, Y. A novel molecularly imprinted material based on magnetic halloysite nanotubes for rapid enrichment of 2, 4-dichlorophenoxyacetic acid in water. *J. Hazard. Mater.* **2014,** *276*, 58-65.

(16) Zhou, C.; Li, H.; Zhou, H.; Wang, H.; Yang, P.; Zhong, S. Water‐compatible halloysite‐imprinted polymer by Pickering emulsion polymerization for the selective recognition of herbicides. *J. sep. sci.* **2015,** *38* (8), 1365-1371.

(17) Hu, X.-j.; Wang, J.-s.; Liu, Y.-g.; Li, X.; Zeng, G.-m.; Bao, Z.-l.; Zeng, X.-x.; Chen, A.-w.; Long, F. Adsorption of chromium (VI) by ethylenediamine-modified cross-linked magnetic chitosan resin: Isotherms, kinetics and thermodynamics. *J. Hazard. Mater.* **2011,** *185* (1), 306-314, DOI: 10.1016/j.jhazmat.2010.09.034.

(18) Huang, D.; Hu, C.; Zeng, G.; Cheng, M.; Xu, P.; Gong, X.; Wang, R.; Xue, W. Combination of Fenton processes and biotreatment for wastewater treatment and soil remediation. *Sci. Total Environ.* **2017,** *574*, 1599-1610.

(19) Cheng, M.; Zeng, G.; Huang, D.; Lai, C.; Xu, P.; Zhang, C.; Liu, Y. Hydroxyl radicals based advanced oxidation processes (AOPs) for remediation of soils contaminated with organic compounds: A review. *Chem. Eng. J.* **2016,** *284*, 582-598, DOI: 10.1016/j.cej.2015.09.001.

(20) Cheng, M.; Zeng, G.; Huang, D.; Lai, C.; Xu, P.; Zhang, C.; Liu, Y.; Wan, J.; Gong, X.; Zhu, Y. Degradation of atrazine by a novel Fenton-like process and assessment the influence on the treated soil. *J. Hazard. Mater.* **2016,** *312*, 184-191, DOI: 10.1016/j.jhazmat.2016.03.033.

(21) Huang, D.-L.; Zeng, G.-M.; Feng, C.-L.; Hu, S.; Jiang, X.-Y.; Tang, L.; Su, F.-F.; Zhang, Y.; Zeng, W.; Liu, H.-L. Degradation of lead-contaminated lignocellulosic waste by Phanerochaete chrysosporium and the reduction of lead toxicity. *Environ Sci. Technol.* **2008,** *42* (13), 4946-4951, DOI: 10.1021/es800072c.

(22) Gao, Y.-q.; Gao, N.-y.; Deng, Y.; Yang, Y.-q.; Ma, Y. Ultraviolet (UV) light-activated persulfate oxidation of sulfamethazine in water. *Chem. Eng. J.* **2012,** *195-196*, 248-253, DOI: 10.1016/j.cej.2012.04.084.

(23) Yang, C.; Chen, H.; Zeng, G.; Yu, G.; Luo, S. Biomass accumulation and control strategies in gas biofiltration. *Biotechnol. Adv.* **2010,** *28* (4), 531-540, DOI: 10.1016/j.biotechadv.2010.04.002.

(24) Polesel, F.; Andersen, H. R.; Trapp, S.; Plósz, B. G. Removal of Antibiotics in Biological Wastewater Treatment Systems A Critical Assessment Using the Activated Sludge Modeling Framework for Xenobiotics (ASM-X). *Environ Sci. Technol.* **2016,** *50* (19), 10316-10334.

(25) Lu, Z.; Zeng, L.; Song, W.; Qin, Z.; Zeng, D.; Xie, C. In situ synthesis of C-TiO_2/g-C_3N_4 heterojunction nanocomposite as highly visible light active photocatalyst originated from effective interfacial charge transfer. *Appl. Catal. B: Environ.* **2017,** *202*, 489-499, DOI: 10.1016/j.apcatb.2016.09.052.

(26) Lai, C.; Wang, M.-M.; Zeng, G.-M.; Liu, Y.-G.; Huang, D.-L.; Zhang, C.; Wang, R.-Z.; Xu, P.; Cheng, M.; Huang, C. Synthesis of surface molecular imprinted TiO_2/graphene photocatalyst and its highly efficient photocatalytic degradation of target pollutant under visible light irradiation. *Appl. Surf. Sci.* **2016,** *390*, 368-376.

(27) Chen, F.; Yang, Q.; Wang, Y.; Zhao, J.; Wang, D.; Li, X.; Guo, Z.; Wang, H.; Deng, Y.; Niu, C.; Zeng, G. Novel ternary heterojunction photcocatalyst of Ag nanoparticles and g-C3N4

nanosheets co-modified BiVO$_4$ for wider spectrum visible-light photocatalytic degradation of refractory pollutant. *Appl. Catal. B: Environ.* **2017,** *205*, 133-147, DOI: 10.1016/j.apcatb.2016.12.017.

(28) Zhou, C. Y.; Lai, C.; Huang, D. L.; Zeng, G. M.; Zhang, C.; Cheng, M.; Hu, L.; Wan, J.; Xiong, W. P.; Wen, M.; Wen, X. F.; Qin, L. Highly porous carbon nitride by supramolecular preassembly of monomers for photocatalytic removal of sulfamethazine under visible light driven. *Appl. Catal. B: Environ.* **2018,** *220*, 202-210, DOI: 10.1016/j.apcatb.2017.08.055.

(29) Li, K.; Han, M.; Chen, R.; Li, S.-L.; Xie, S.-L.; Mao, C.; Bu, X.; Cao, X.-L.; Dong, L.-Z.; Feng, P.; Lan, Y.-Q. Hexagonal@Cubic CdS Core@Shell Nanorod Photocatalyst for Highly Active Production of H2 with Unprecedented Stability. *Adv. Mater.* **2016,** *28* (40), 8906-8911, DOI: 10.1002/adma.201601047.

(30) Yang, S.-F.; Niu, C.-G.; Huang, D.; Zhang, H.; Liang, C.; Zeng, G. SrTiO3 nanocubes decorated with Ag/AgCl nanoparticles as photocatalysts with enhanced visible-light photocatalytic activity towards the degradation of dyes, phenol and bisphenol A. *Environmental Science: Nano* **2017**. 4(3): 585-595.

(31) Wang, C.-Y.; Zhang, X.; Song, X.-N.; Wang, W.-K.; Yu, H.-Q. Novel Bi12O15Cl6Photocatalyst for the Degradation of Bisphenol A under Visible-Light Irradiation. *ACS Appl. Mater. Interfaces* **2016,** *8* (8), 5320-5326, DOI: 10.1021/acsami.5b12092.

(32) Li, H.; Zhang, L. Photocatalytic performance of different exposed crystal facets of BiOCl. *Opin. Green Sus. Chem.* **2017**, DOI: 10.1016/j.cogsc.2017.05.005.

(33) Li, J.; Li, H.; Zhan, G.; Zhang, L. Solar Water Splitting and Nitrogen Fixation with Layered Bismuth Oxyhalides. *Accounts Chem. Res.* **2017,** *50* (1), 112-121, DOI:

10.1021/acs.accounts.6b00523.

(34) Tang, L.; Zeng, G.-M.; Shen, G.-L.; Li, Y.-P.; Zhang, Y.; Huang, D.-L. Rapid detection of picloram in agricultural field samples using a disposable immunomembrane-based electrochemical sensor. *Environ. Sci. Technol.* **2008,** *42* (4), 1207-1212, DOI: 10.1021/es7024593.

(35) Liu, J.; Zhao, H.; Wu, M.; Van der Schueren, B.; Li, Y.; Deparis, O.; Ye, J.; Ozin, G. A.; Hasan, T.; Su, B.-L. Slow Photons for Photocatalysis and Photovoltaics. *Adv. Mater.* **2017,** *29* (17), 1605349, DOI: 10.1002/adma.201605349.

(36) Li, H.; Qin, F.; Yang, Z.; Cui, X.; Wang, J.; Zhang, L. New Reaction Pathway Induced by Plasmon for Selective Benzyl Alcohol Oxidation on BiOCl Possessing Oxygen Vacancies. *J. Am. Chem. Soc.* **2017,** *139* (9), 3513-3521, DOI: 10.1021/jacs.6b12850.

(37) Li, J.; Zhao, K.; Yu, Y.; Zhang, L. Facet-Level Mechanistic Insights into General Homogeneous Carbon Doping for Enhanced Solar-to-Hydrogen Conversion. *Adv. Funct. Mater.* **2015,** *25* (14), 2189-2201, DOI: 10.1002/adfm.201404178.

(38) Wang, L.; Shang, J.; Hao, W.; Jiang, S.; Huang, S.; Wang, T.; Sun, Z.; Du, Y.; Dou, S.; Xie, T. A dye-sensitized visible light photocatalyst-$Bi_{24}O_{31}Cl_{10}$. *Sci. Rep.* **2014,** *4*, 7384.

(39) Meng, X.; Zhang, G.; Li, N. $Bi_{24}Ga_2O_{39}$ for visible light photocatalytic reduction of Cr(VI): Controlled synthesis, facet-dependent activity and DFT study. *Chem. Eng. J.* **2017,** *314* (Supplement C), 249-256, DOI: https://doi.org/10.1016/j.cej.2016.12.090.

(40) Li, J.; Wu, X.; Pan, W.; Zhang, G.; Chen, H. Vacancy-Rich Monolayer BiO2−x as a Highly Efficient UV, Visible, and Near-Infrared Responsive Photocatalyst. *Angewandte Chemie*, n/a-n/a, DOI: 10.1002/ange.201708709.

(41) Wang, C.-Y.; Zhang, X.; Qiu, H.-B.; Wang, W.-K.; Huang, G.-X.; Jiang, J.; Yu, H.-Q.

Photocatalytic degradation of bisphenol A by oxygen-rich and highly visible-light responsive $Bi_{12}O_{17}Cl_2$ nanobelts. *Appl. Catal. B: Environ.* **2017,** *200*, 659-665, DOI: 10.1016/j.apcatb.2016.07.054.

(42) Li, H.; Zhang, L. Oxygen vacancy induced selective silver deposition on the {001} facets of BiOCl single-crystalline nanosheets for enhanced Cr(vi) and sodium pentachlorophenate removal under visible light. *Nanoscale* **2014,** *6* (14), 7805, DOI: 10.1039/c4nr01315h.

(43) Li, J.; Zhan, G.; Yu, Y.; Zhang, L. Superior visible light hydrogen evolution of Janus bilayer junctions via atomic-level charge flow steering. *Nature Commun.* **2016,** *7*, 11480, DOI: 10.1038/ncomms11480.

(44) Xiao, X.; Jiang, J.; Zhang, L. Selective oxidation of benzyl alcohol into benzaldehyde over semiconductors under visible light: The case of $Bi_{12}O_{17}Cl_2$ nanobelts. *Appl. Catal. B: Environ.* **2013,** *142*, 487-493.

(45) Wen, X.-J.; Niu, C.-G.; Ruan, M.; Zhang, L.; Zeng, G.-M. AgI nanoparticles-decorated CeO_2 microsheets photocatalyst for the degradation of organic dye and tetracycline under visible-light irradiation. *J. Colloid Interf. Sci.* **2017,** *497*, 368-377, DOI: 10.1016/j.jcis.2017.03.029.

(46) Wan, Z.; Zhang, G. Synthesis and facet-dependent enhanced photocatalytic activity of Bi_2SiO_5/AgI nanoplate photocatalysts. *J. Mater. Chem. A* **2015,** *3* (32), 16737-16745, DOI: 10.1039/C5TA03465E.

(47) Zhang, L.; Hu, C.; Ji, H. p-AgI anchored on {001} facets of n-$Bi_2O_2CO_3$ sheets with enhanced photocatalytic activity and stability. *Appl. Catal. B: Environ.* **2017,** *205*, 34-41, DOI: 10.1016/j.apcatb.2016.12.015.

(48) Ning, S.; Lin, H.; Tong, Y.; Zhang, X.; Lin, Q.; Zhang, Y.; Long, J.; Wang, X. Dual couples

Bi metal depositing and Ag@AgI islanding on BiOI 3D architectures for synergistic bactericidal mechanism of E. coli under visible light. *Appl. Catal. B: Environ.* **2017,** *204*, 1-10, DOI: 10.1016/j.apcatb.2016.11.006.

(49) Wang, C.-Y.; Zhang, X.; Qiu, H.-B.; Huang, G.-X.; Yu, H.-Q. Bi24O31Br10 nanosheets with controllable thickness for visible–light–driven catalytic degradation of tetracycline hydrochloride. *Appl. Catal. B: Environ.* **2017,** *205*, 615-623, DOI: 10.1016/j.apcatb.2017.01.015.

(50) He, G.; Xing, C.; Xiao, X.; Hu, R.; Zuo, X.; Nan, J. Facile synthesis of flower-like $Bi_{12}O_{17}Cl_2$/β-Bi_2O_3 composites with enhanced visible light photocatalytic performance for the degradation of 4-tert-butylphenol. *Appl. Catal. B: Environ.* **2015,** *170-171*, 1-9, DOI: 10.1016/j.apcatb.2015.01.015.

(51) Huang, H.; Xiao, K.; He, Y.; Zhang, T.; Dong, F.; Du, X.; Zhang, Y. In situ assembly of BiOI@$Bi_{12}O_{17}Cl_2$ p-n junction: charge induced unique front-lateral surfaces coupling heterostructure with high exposure of BiOI {001} active facets for robust and nonselective photocatalysis. *Appl. Catal. B: Environ.* **2016,** *199*, 75-86, DOI: 10.1016/j.apcatb.2016.06.020.

(52) Wang, T.; Quan, W.; Jiang, D.; Chen, L.; Li, D.; Meng, S.; Chen, M. Synthesis of redox-mediator-free direct Z-scheme AgI/WO3 nanocomposite photocatalysts for the degradation of tetracycline with enhanced photocatalytic activity. *Chem. Eng. J.* **2016,** *300*, 280-290, DOI: 10.1016/j.cej.2016.04.128.

(53) Chen, F.; Yang, Q.; Sun, J.; Yao, F.; Wang, S.; Wang, Y.; Wang, X.; Li, X.; Niu, C.; Wang, D.; Zeng, G. Enhanced Photocatalytic Degradation of Tetracycline by AgI/$BiVO_4$ Heterojunction under Visible-Light Irradiation: Mineralization Efficiency and Mechanism. *ACS Appl. Mater. Inter.* **2016,** *8* (48), 32887-32900, DOI: 10.1021/acsami.6b12278.

(54) Hao, L.; Huang, H.; Guo, Y.; Du, X.; Zhang, Y. Bismuth oxychloride homogeneous phasejunction BiOCl/$Bi_{12}O_{17}Cl_2$ with unselectively efficient photocatalytic activity and mechanism insight. *Appl. Surf. Sci.* **2017,** *420* (Supplement C), 303-312, DOI: https://doi.org/10.1016/j.apsusc.2017.05.076.

(55) Cheng, H.; Wang, W.; Huang, B.; Wang, Z.; Zhan, J.; Qin, X.; Zhang, X.; Dai, Y. Tailoring AgI nanoparticles for the assembly of AgI/BiOI hierarchical hybrids with size-dependent photocatalytic activities. *J. Mater. Chem. A* **2013,** *1* (24), 7131-7136.

(56) Wang, J.; Tang, L.; Zeng, G.; Deng, Y.; Liu, Y.; Wang, L.; Zhou, Y.; Guo, Z.; Wang, J.; Zhang, C. Atomic scale g-C_3N_4/Bi_2WO_6 2D/2D heterojunction with enhanced photocatalytic degradation of ibuprofen under visible light irradiation. *Appl. Catal. B: Environ.* **2017,** *209*, 285-294, DOI: 10.1016/j.apcatb.2017.03.019.

(57) Zhang, L.; Niu, C.-G.; Xie, G.; Wen, X.-J.; Zhang, X.-G.; Zeng, G. Controlled growth of BiOCl with large {010} facets for dye self-photosensitization photocatalytic fuel cells application. *ACS Sustainable Chem. Eng.* **2017**.

(58) Zhang, C.; Lai, C.; Zeng, G.; Huang, D.; Tang, L.; Yang, C.; Zhou, Y.; Qin, L.; Cheng, M. Nanoporous Au-based chronocoulometric aptasensor for amplified detection of Pb 2+ using DNAzyme modified with Au nanoparticles. *Biosens. Bioelectron.* **2016,** *81*, 61-67.

(59) Zeng, G.; Zhang, C.; Huang, D.; Lai, C.; Tang, L.; Zhou, Y.; Xu, P.; Wang, H.; Qin, L.; Cheng, M. Practical and regenerable electrochemical aptasensor based on nanoporous gold and thymine-Hg^{2+}-thymine base pairs for Hg^{2+} detection. *Biosens. Bioelectron.* **2017,** *90*, 542-548.

(60) Deng, Y.; Tang, L.; Zeng, G.; Zhu, Z.; Yan, M.; Zhou, Y.; Wang, J.; Liu, Y.; Wang, J. Insight into highly efficient simultaneous photocatalytic removal of Cr(VI) and 2,4-diclorophenol under

visible light irradiation by phosphorus doped porous ultrathin g-C_3N_4 nanosheets from aqueous media: Performance and reaction mechanism. *Appl. Catal. B: Environ.* **2017,** *203*, 343-354, DOI: 10.1016/j.apcatb.2016.10.046.

(61) Guo, C.; Xu, J.; Wang, S.; Zhang, Y.; He, Y.; Li, X. Photodegradation of sulfamethazine in an aqueous solution by a bismuth molybdate photocatalyst. *Catal. Sci. Technol.* **2013,** *3* (6), 1603, DOI: 10.1039/c3cy20811g.

(62) Dong, F.; Li, C.; He, G.; Chen, X.; Mao, X. Kinetics and degradation pathway of sulfamethazine chlorination in pilot-scale water distribution systems. *Chem. Eng. J.* **2017,** *321*, 521-532, DOI: 10.1016/j.cej.2017.03.130.

(63) Chen, F.; Yang, Q.; Li, X.; Zeng, G.; Wang, D.; Niu, C.; Zhao, J.; An, H.; Xie, T.; Deng, Y. Hierarchical assembly of graphene-bridged Ag_3PO_4/Ag/$BiVO_4$ (040) Z-scheme photocatalyst: An efficient, sustainable and heterogeneous catalyst with enhanced visible-light photoactivity towards tetracycline degradation under visible light irradiation. *Appl. Catal. B: Environ.* **2017,** *200*, 330-342, DOI: 10.1016/j.apcatb.2016.07.021.

(64) Chen, F.; Yang, Q.; Wang, S.; Yao, F.; Sun, J.; Wang, Y.; Zhang, C.; Li, X.; Niu, C.; Wang, D.; Zeng, G. Graphene oxide and carbon nitride nanosheets co-modified silver chromate nanoparticles with enhanced visible-light photoactivity and anti-photocorrosion properties towards multiple refractory pollutants degradation. *Appl. Catal. B: Environ.* **2017,** *209*, 493-505, DOI: 10.1016/j.apcatb.2017.03.026.

(65) Cheng, M.; Zeng, G.; Huang, D.; Lai, C.; Liu, Y.; Xu, P.; Zhang, C.; Wan, J.; Hu, L.; Xiong, W. Salicylic acid–methanol modified steel converter slag as heterogeneous Fenton-like catalyst for enhanced degradation of alachlor. *Chem. Eng. J.* **2017,** *327*, 686-693.

(66) Chen, F.; Yang, Q.; Zhong, Y.; An, H.; Zhao, J.; Xie, T.; Xu, Q.; Li, X.; Wang, D.; Zeng, G. Photo-reduction of bromate in drinking water by metallic Ag and reduced graphene oxide (RGO) jointly modified BiVO 4 under visible light irradiation. *Water Res.* **2016,** *101*, 555-563, DOI: 10.1016/j.watres.2016.06.006.

(67) Deng, Y.; Tang, L.; Zeng, G.; Feng, C.; Dong, H.; Wang, J.; Feng, H.; Liu, Y.; Zhou, Y.; Pang, Y. Plasmonic resonance excited dual Z-scheme BiVO4/Ag/Cu2O nanocomposite: synthesis and mechanism for enhanced photocatalytic performance in recalcitrant antibiotic degradation. *Environmental Science: Nano* **2017**, DOI: 10.1039/c7en00237h.

(68) Tian, N.; Zhang, Y.; Li, X.; Xiao, K.; Du, X.; Dong, F.; Waterhouse, G. I. N.; Zhang, T.; Huang, H. Precursor-reforming protocol to 3D mesoporous g-C_3N_4 established by ultrathin self-doped nanosheets for superior hydrogen evolution. *Nano Energy* **2017,** *38*, 72-81, DOI: 10.1016/j.nanoen.2017.05.038.

Figure captions:

Figure 1. XRD patterns of samples AgI, $Bi_{12}O_{17}Cl_2$, and AgI/$Bi_{12}O_{17}Cl_2$ (14%, 25%, and 40%).

Figure 2. The XPS spectra of 25% AgI/$Bi_{12}O_{17}Cl_2$ (a) survey spectra, (b) high resolution Ag 3d, (c) high resolution I 3d, (d) high resolution Bi 4f, (e) high resolution Cl 2p, and (f) high resolution O 1s.

Figure 3. SEM images of (a) $Bi_{12}O_{17}Cl_2$; (b-c) 25% AgI/$Bi_{12}O_{17}Cl_2$; and (d to h) corresponding elemental maps of 25% AgI/$Bi_{12}O_{17}Cl_2$.

Figure 4. (a-c) TEM images of AgI, $Bi_{12}O_{17}Cl_2$ and 25% AgI/$Bi_{12}O_{17}Cl_2$, respectively, (d) High resolution TEM image of 25% AgI/$Bi_{12}O_{17}Cl_2$.

Figure 5. (a) UV-vis adsorption spectra of samples, and (b) The plots of $(ahv)^{1/2}$ *vs* photon energy (hv) for $Bi_{12}O_{17}Cl_2$ and the plots of $(ahv)^2$ *vs* photon energy (hv) for AgI.

Figure 6. (a) Photocurrent transient measurement and (b) electrochemical impedance spectra of photocatalysts.

Figure 7. (a) Photodegradation rate of SMZ on different photocatalyst, (b) Kinetic fit of the degradation of SMZ on different photocatalyst samples, (c) effect of initial concentration of SMZ on 25% AgI/$Bi_{12}O_{17}Cl_2$, and (d) Kinetic fit of the initial concentration of SMZ on 25% AgI/$Bi_{12}O_{17}Cl_2$.

Figure 8. The TOC degraded efficiencies of SMZ on 25% AgI/$Bi_{12}O_{17}Cl_2$.

Figure 9. The cycle runs in the photodegradation of SMZ over 25% AgI/$Bi_{12}O_{17}Cl_2$.

Figure 10. The photocatalytic degradation plots of SMZ over (a) $Bi_{12}O_{17}Cl_2$, (b) 25% $AgI/Bi_{12}O_{17}Cl_2$ with the addition of hole, $\bullet O_2^-$ and •OH radical scavenger under visible light irradiation; ESR spectra of $AgI/Bi_{12}O_{17}Cl_2$ dispersion under both the dark and visible light irradiation (> 420 nm) condition: (c) in methanol dispersion for DMPO-$\bullet O_2^-$, (d) in aqueous dispersion for DMPO-•OH.

Figure 11. Proposed SMZ photodegradation pathway by 25% $AgI/Bi_{12}O_{17}Cl_2$ photocatalyst.

Figure 12. Schematic of the mechanism of the photocatalytic SMZ degradation on 25% $AgI/Bi_{12}O_{17}Cl_2$.

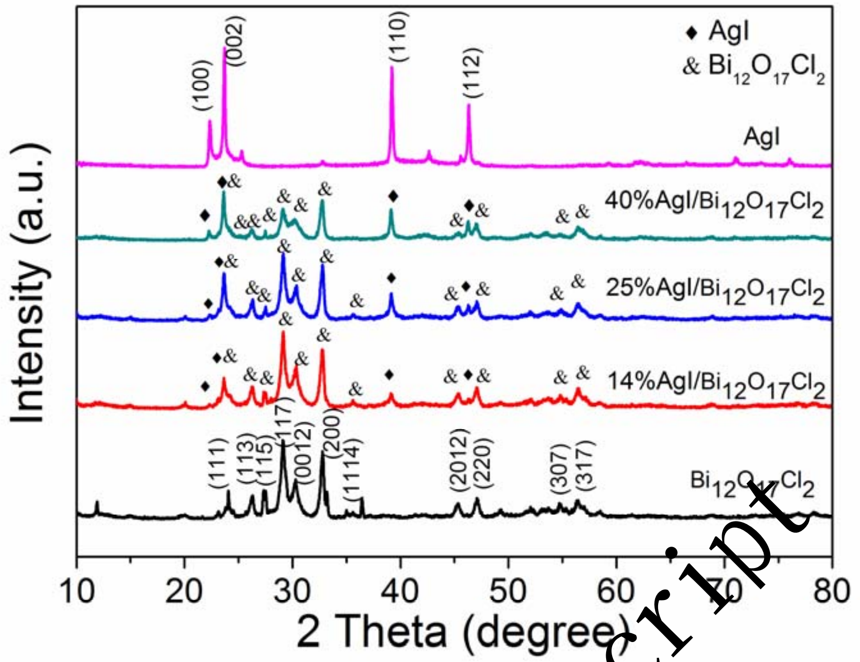

Figure 1. XRD patterns of samples AgI, $Bi_{12}O_{17}Cl_2$, and AgI/$Bi_{12}O_{17}Cl_2$ (14%, 25%, and 40%).

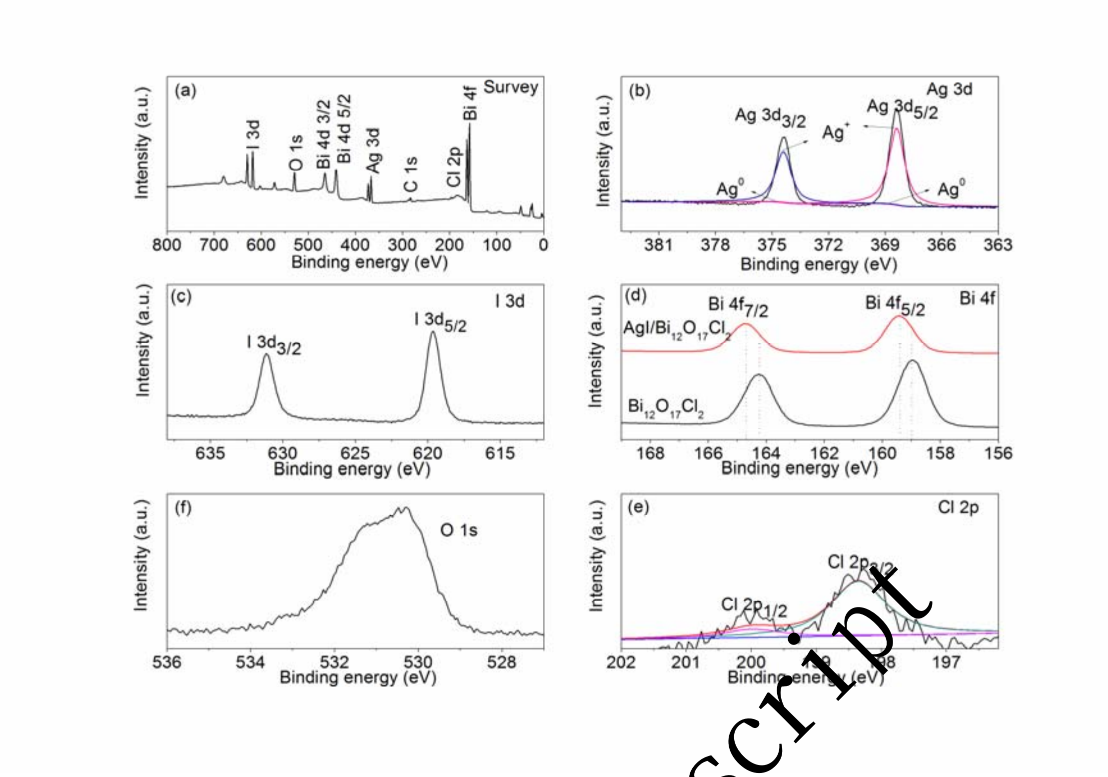

Figure 2. The XPS spectra of 25% AgI/Bi$_{12}$O$_{17}$Cl$_2$ (a) survey spectra, (b) high resolution Ag 3d, (c) high resolution I 3d, (d) high resolution Bi 4f, (e) high resolution Cl 2p, and (f) high resolution O 1s.

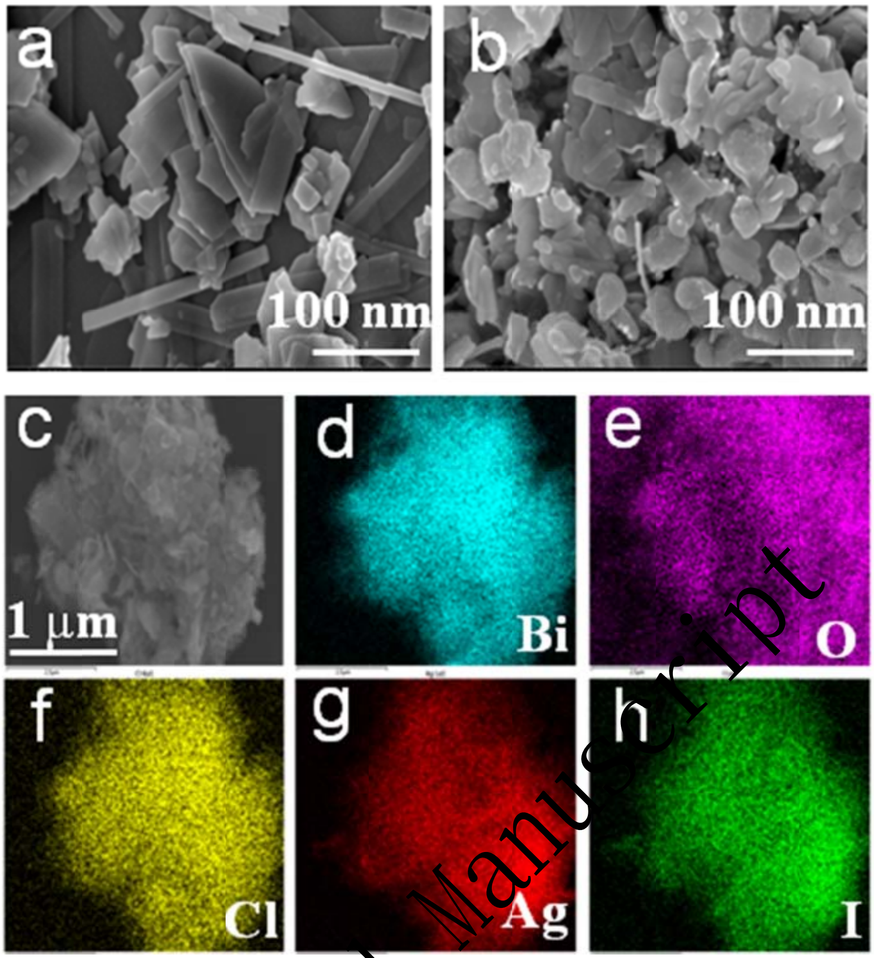

Figure 3. SEM images of (a) $Bi_{12}O_{17}Cl_2$; (b-c) 25% AgI/$Bi_{12}O_{17}Cl_2$; and (d to h) corresponding elemental maps of 25% AgI/$Bi_{12}O_{17}Cl_2$.

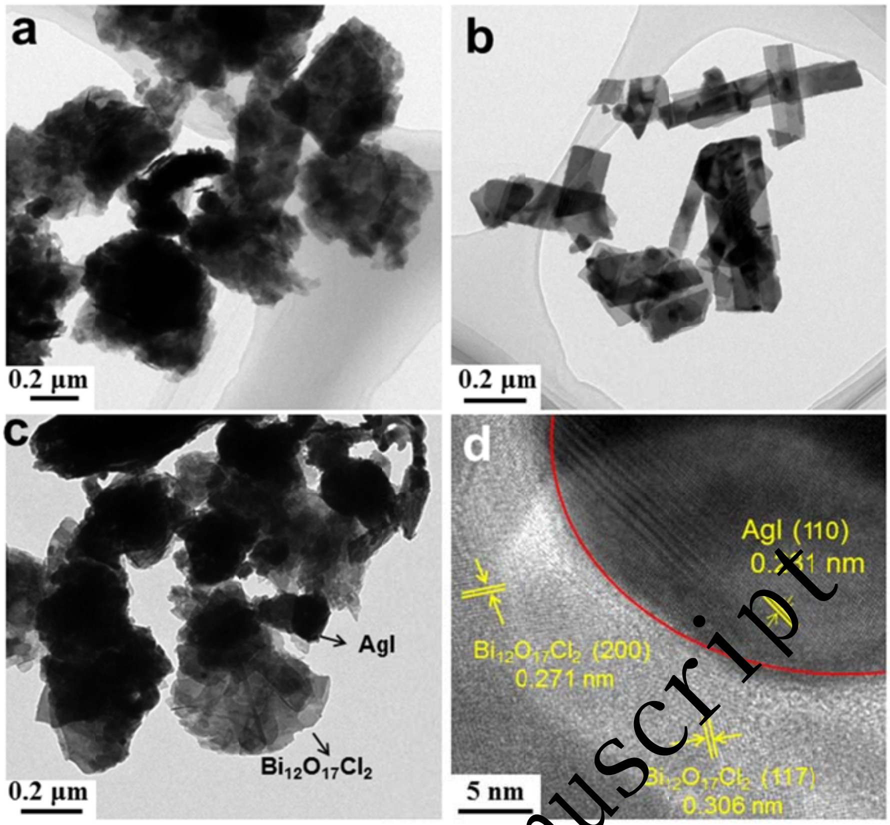

Figure 4. (a-c) TEM images of AgI, $Bi_{12}O_{17}Cl_2$ and 25% AgI/$Bi_{12}O_{17}Cl_2$, respectively, (d) High resolution TEM image of 25% AgI/$Bi_{12}O_{17}Cl_2$.

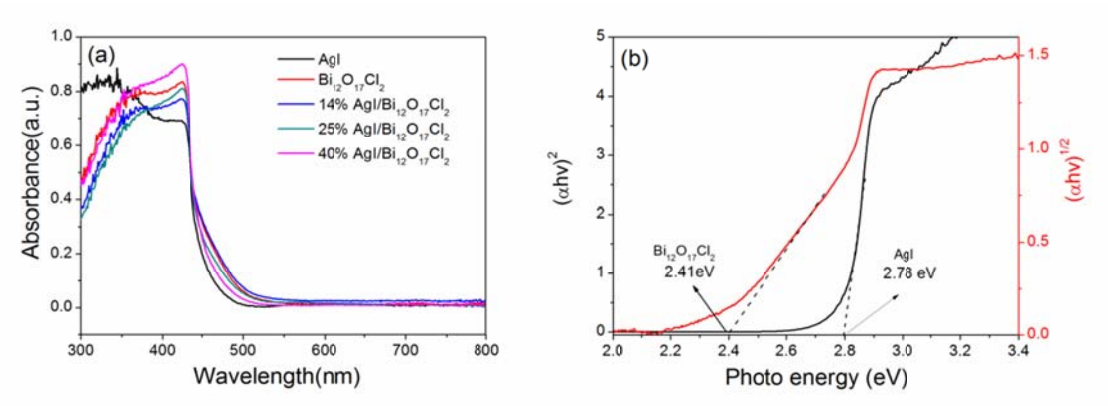

Figure 5. (a) UV-vis adsorption spectra of samples, and (b) The plots of *$(\alpha hv)^{1/2}$* *vs* photon energy *(hv)* for $Bi_{12}O_{17}Cl_2$ and the plots of *$(\alpha hv)^2$* *vs* photon energy *(hv)* for AgI.

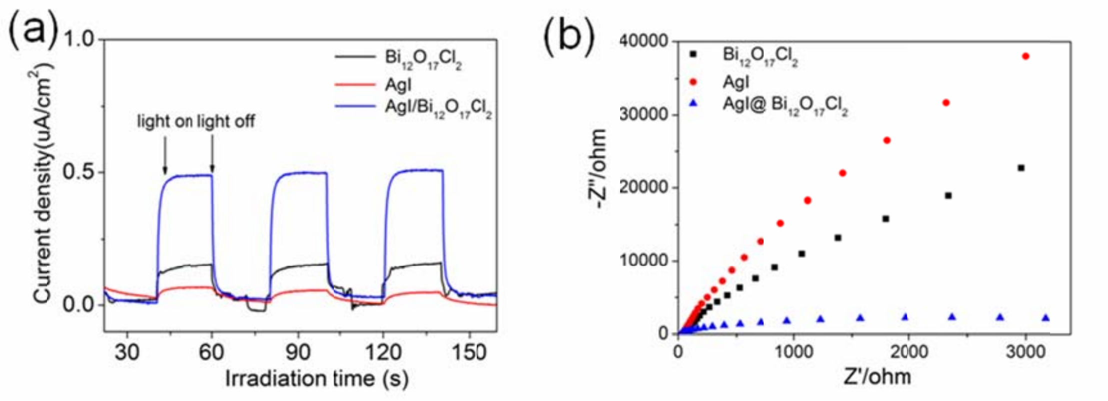

Figure 6. (a) Photocurrent transient measurement and (b) electrochemical impedance spectra of photocatalysts.

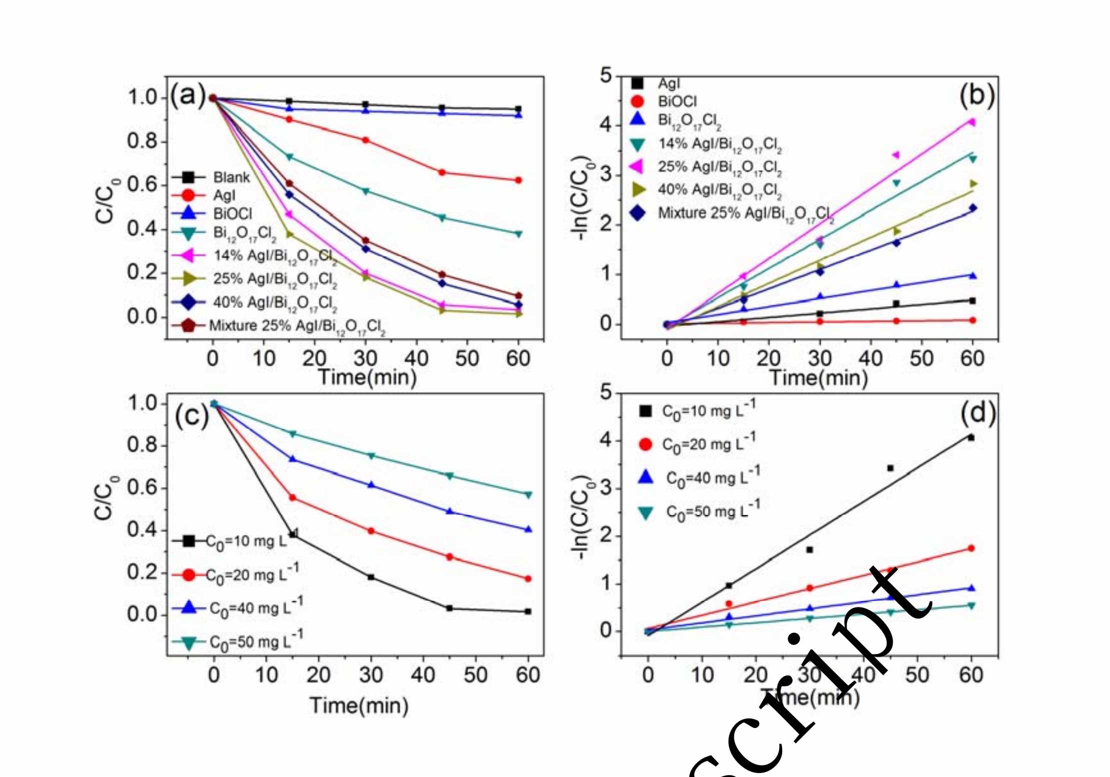

Figure 7. (a) Photodegradation rate of SMZ on different photocatalyst, (b) Kinetic fit of the degradation of SMZ on different photocatalyst samples, (c) effect of initial concentration of SMZ on 25% AgI/$Bi_{12}O_{17}Cl_2$, and (d) Kinetic fit of the initial concentration of SMZ on 25% AgI/$Bi_{12}O_{17}Cl_2$.

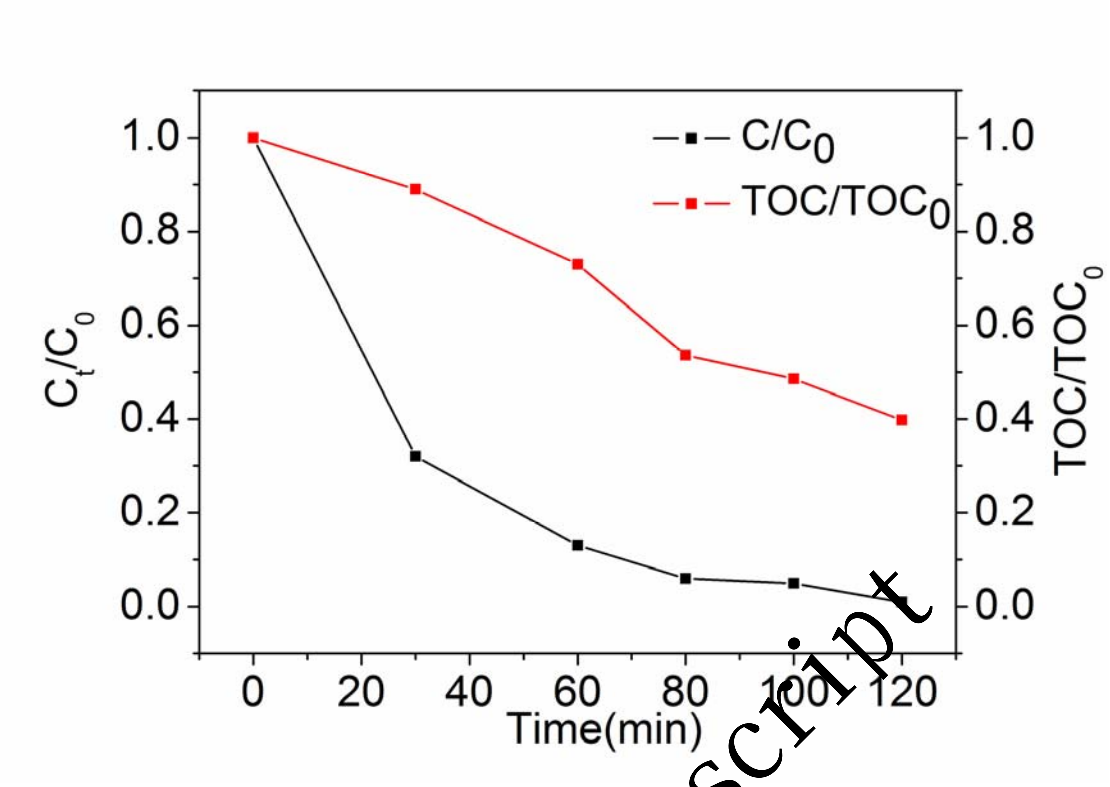

Figure 8. The TOC degraded efficiencies of SMZ on 25% $AgI/Bi_{12}O_{17}Cl_2$.

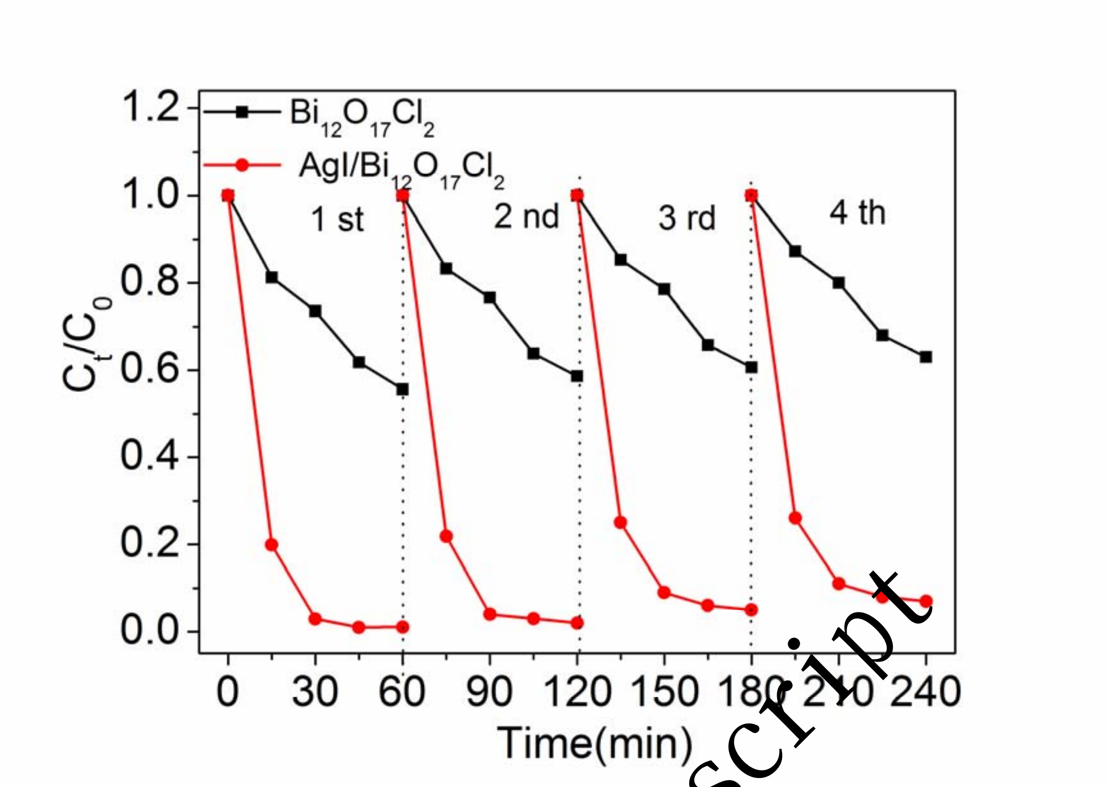

Figure 9. The cycle runs in the photodegradation of SMZ over 25% $AgI/Bi_{12}O_{17}Cl_2$.

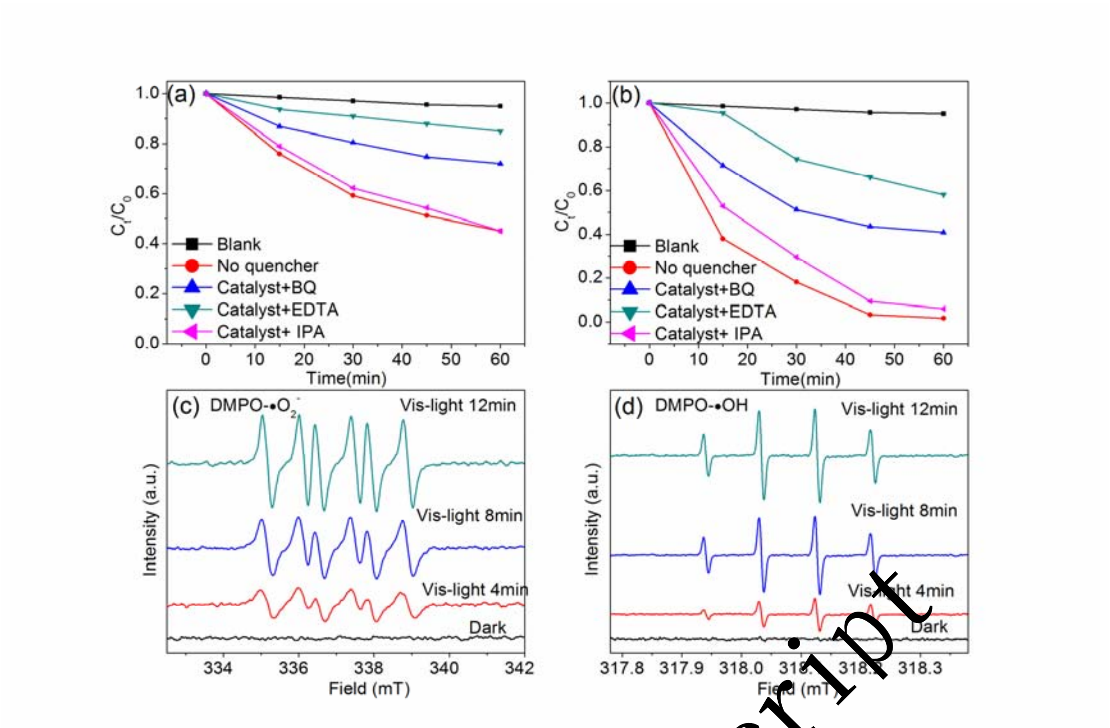

Figure 10. The photocatalytic degradation plots of SMZ over (a) $Bi_{12}O_{17}Cl_2$, (b) 25% $AgI/Bi_{12}O_{17}Cl_2$ with the addition of hole, •O_2 and •OH radical scavenger under visible light irradiation; ESR spectra of 25% $AgI/Bi_{12}O_{17}Cl_2$ dispersion under both the dark and visible light irradiation (> 420 nm) condition: (c) in methanol dispersion for DMPO-•O_2^-, (d) in aqueous dispersion for DMPO-•OH.

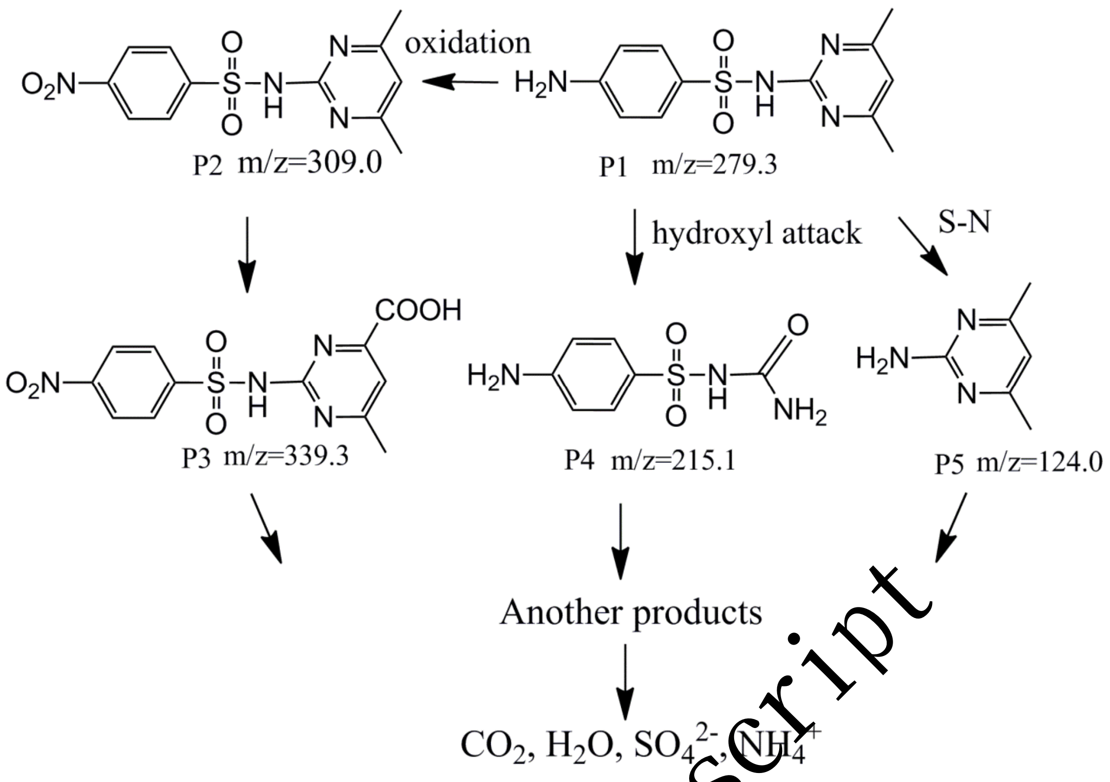

Figure 11. Proposed SMZ photodegradation pathway by 25% AgI/Bi$_{12}$O$_{17}$Cl$_2$ photocatalyst.

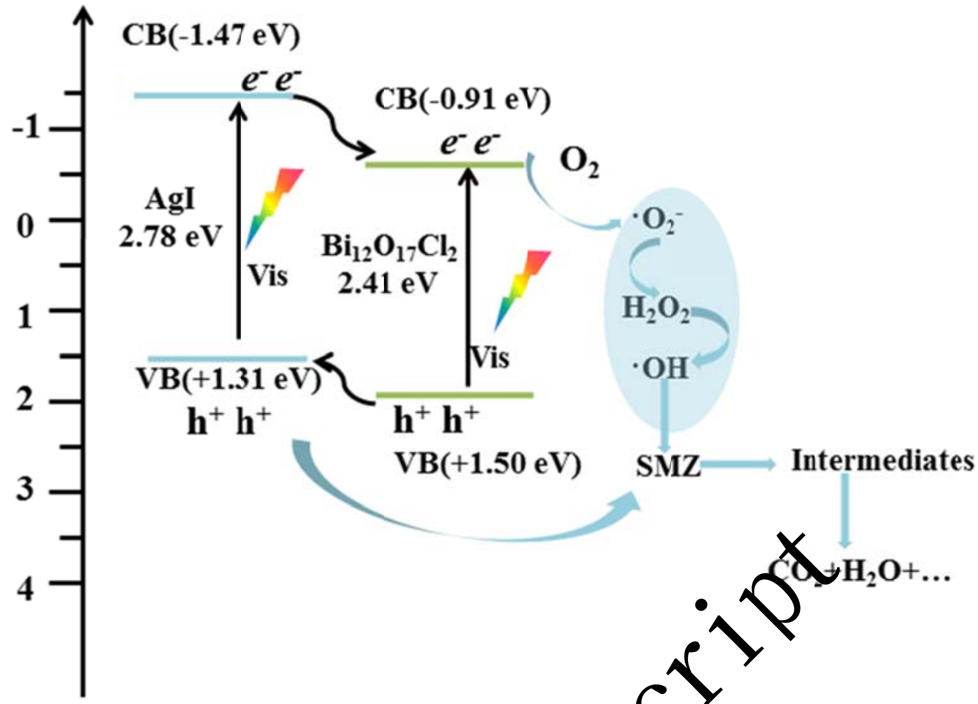

Figure 12. Schematic of the mechanism of the photocatalytic SMZ degradation on 25% $AgI/Bi_{12}O_{17}Cl_2$.